Hindawi
International Journal of Aerospace Engineering
Volume 2024, Article ID 2284914, 19 pages
https://doi.org/10.1155/2024/2284914

Research Article

Machine Learning-Based Backpressure Unstart Prediction and Warning Method for Combined Cycle Engine Hypersonic Inlet-Oriented Wide Speed Range

Ke Min, Tanbao Hong, Zejun Cai, Lianchen Yu, Chengxiang Zhu, and Jianping Zeng

School of Aeronautics and Astronautics, Xiamen University, Xiamen 361102, China

Correspondence should be addressed to Chengxiang Zhu; chengxiang.zhu@xmu.edu.cn and Jianping Zeng; jpzeng@xmu.edu.cn

Received 27 June 2023; Revised 25 January 2024; Accepted 9 February 2024; Published 29 February 2024

Academic Editor: Gautam Choubey

Inlet unstart prediction and warning are strictly crucial to the operation of hypersonic engines, especially for combined cycle engines where implementation across a wide speed range poses significant challenges. This paper proposes a realization method that involves constructing the conditions of critical backpressure ratios for the inlet unstart and unstart warning states within a wide speed range and establishing the backpressure prediction models for each engine mode. The detection of the unstart and unstart warning states is achieved by predicting the backpressure ratio at the exit of the isolator and comparing it to the critical backpressure ratios. To achieve this, numerical simulations for a three-dimensional inward-turning multiducted hypersonic combined inlet at various Mach numbers and backpressure ratios are carried out to obtain the dataset of surface pressure. A 10-fold cross-validation support vector machine (10-CV SVM) is used to solve the unstart boundary of surface pressure, and an unstart margin is set to determine the unstart warning boundary. A back propagation (BP) neural network is constructed to estimate the critical backpressure ratios at each working point within a wide speed range. The data information of surface pressure on the boundaries is used as the input for the predictions. The overall average regression correlation coefficient approaches 0.99 on the test dataset at each working point. The backpressure prediction models are established by the one-dimensional convolutional neural network (1D-CNN). Only 2 to 4 measurement points of surface pressure are considered for cross-validation evaluation, and the mean absolute percentage error is between 4% and 8% with the average prediction time not exceeding 2 ms. Finally, the proposed method and prediction models are validated by wind tunnel experimental data.

1. Introduction

With the rapid development of hypersonic propulsion technology, wide-speed hypersonic vehicles have gained widespread attention in research on combustion and propulsion [1], flight control and navigation [2–4], and aerodynamic performance and structural design [5, 6]. Combined cycle engines have become a necessity to meet the demands for wide speed range flights with its performance advantages [7–9]. As the key component, the inlet directly affects the engine operating conditions. It is well known that the unstart phenomenon is one of the most important issues of the hypersonic inlet, which should be prevented [10] or taken effective measures to realize the restart when falling into the unstart state [11–13]. However, once the inlet unstart occurs during flight, it will increase the working burden of the hypersonic engine, and the hysteresis phenomena in the restarting process of the hypersonic inlet are widespread [14]. Especially in some certain cases, it is even impossible to restart during the engine operation [15]. Moreover, the current research on inlet unstart prediction and warning is mainly limited to two-dimensional inlets and relatively single speed range operating conditions, which is not sufficient to meet the requirements of combined cycle engines under wide speed range flight conditions.

Hypersonic inlets have evolved from binary, side pressure, and axisymmetric designs to three-dimensional internal contraction designs. Owing to the advantages of strong

compression, high flow capture, and small upwind area, three-dimensional inward-turning combined inlets have become the current developmental trend in hypersonic inlets. Examples include the Falcon inlet based on the variable section design method [16], ACCII (advanced combined circle integrated inlet) in the "Trijet" scheme with streamtracking technology [17], and the SR-72 inlet with double waverider design. Nevertheless, due to the more complex flow field of the inward-turning combined inlet, there are still great challenges in the unstart mechanism and prediction, which involves more flow parameters and interactions. Therefore, it is vital to provide a method for the unstart prediction and warning of hypersonic combined inlets with a wide speed range.

Numerous studies [18–20] have shown that the causes of the unstart conditions are very complex for hypersonic inlets, making the prevention of the unstart extremely challenging. Ref. [20] mentioned that the large internal contraction ratio, high backpressure, excessive heat release, and low Mach number are all the causes of hypersonic inlet unstart. Among them, the improper control of backpressure has become the dominant factor. Wagner et al. [21, 22] pointed out that for the unstart phenomenon due to increased backpressure, shock-induced separation plays a leading role and moves along the isolator towards the inlet, causing unstart to occur. Su and Zhang [23] studied the impact of different backpressure ratios on the flow unsteadiness in isolators based on unsteady simulations. High backpressure can make the flow field in the isolator easily unstable, and the oscillation resistance increases sharply. Tan et al. [24] experimentally investigated the entire process of two-dimensional hypersonic inlets from start to unstart. The occurrence process of unstart can be divided into four stages: shock train is located near the combustor, propagates to the isolator, separates to reach the throat, and finally causes unstart. This makes it possible to detect and predict the unstart state of the inlet based on pressure signals, which can provide help for indicating the unstart process [25]. In summary, the effects of backpressure to the inlet stability are crucial, as the pressure changes within the inlet tunnels are directly influenced from the combustor, thus being able to reveal the unstart condition of hypersonic inlets.

At present, the unstart detection methods of the inlet can be divided into two categories: the parametric analysis of pressure instantaneous information and the pattern classification of the pressure steady-state information [20]. The former is based on the analysis of inlet pressure spectrum signals for precursor prediction. It includes the cumulative sum algorithm (CUSUM) [26], general likelihood ratio algorithm (GLR) [26], recursive Fourier transform (RFT) algorithm [27], high-frequency pressure measurements [28], and information fusion [29]. While these above methods have shown promising results in detecting unstart precursors, they are primarily based on wind tunnel experiments, which are relatively difficult to conduct. In recent years, the advancement of computational fluid dynamics (CFD) technology has provided a mature approach for obtaining inlet pressure data [30]. It can provide effective help for the research of the latter.

As the intensive application of machine learning methods in fluid mechanics [31], pattern classification has been applied more frequently in the recognition of inlet unstart state. Based on a certain amount of pressure sample data, machine learning can train a model with high accuracy to recognize inlet unstart through classification method. Yu et al. [32] used the machine learning method to classify the start and unstart states of the inlet for the first time and summarized the optimal classification criteria for the inlet unstart based on the support vector machine recursive feature elimination (SVM-RFE) algorithm and Fisher's linear discriminant (FLD) analysis. Following that, Chang et al. [33] used the SVM classification algorithm to solve the operating mode classification problems of the hypersonic inlets. Additionally, the problems of the classification accuracy of inlet start/unstart with the influence of sensor noise and the limited CFD training data costs were also investigated separately [34, 35]. Zheng et al. [36] also implemented the optimization classification of hypersonic inlet start/unstart based on the manifold learning algorithm. It can be seen that the relevant research on the recognition of inlet unstart state combined with machine learning methods is relatively mature, which proves the effectiveness of this approach. This is attributed to the significant variations in surface pressure along the inlet ducts between the start and unstart states, and the mentioned method is able to discriminate the data based on the significant pressure features. However, it is worth noting that there has been no further research on the inlet unstart warning.

To achieve the unstart prediction and warning of hypersonic combined inlets for a wide speed range, this study proposes a prevention method for backpressure unstart based on machine learning. This method uses the BP neural network to construct the regression mapping relationship between the surface pressure coefficient and the backpressure ratio for each working point during engine operation. To complete the predictions of the critical backpressure ratios of the inlet unstart and unstart states, the pressure information at the unstart boundary and unstart warning boundary determined by 10-CV SVM and unstart margin is used as their regression inputs. Based on this, the conditions of critical backpressure ratios are established by interpolating and curves fitting over a wide speed range. Moreover, the backpressure prediction models for three engine modes (turbine, ejector ramjet, and scramjet modes) are reconstructed by 1D-CNN based on the extraction of optimal surface pressure measurement points. By using several surface pressure measurement points along the inlet, the prediction of the backpressure ratio at the exit of the isolator is completed by the prediction models. Subsequently, this is followed by a judgment on the inlet unstart and unstart warning based on the critical conditions.

The main contributions of this paper can be summarized as follows:

(1) In comparison with existing research, a backpressure unstart prediction and warning method of the inlet is proposed. Its advantages rely only on several pressure measurement points, with short prediction time, acting in wide speed range. The method can

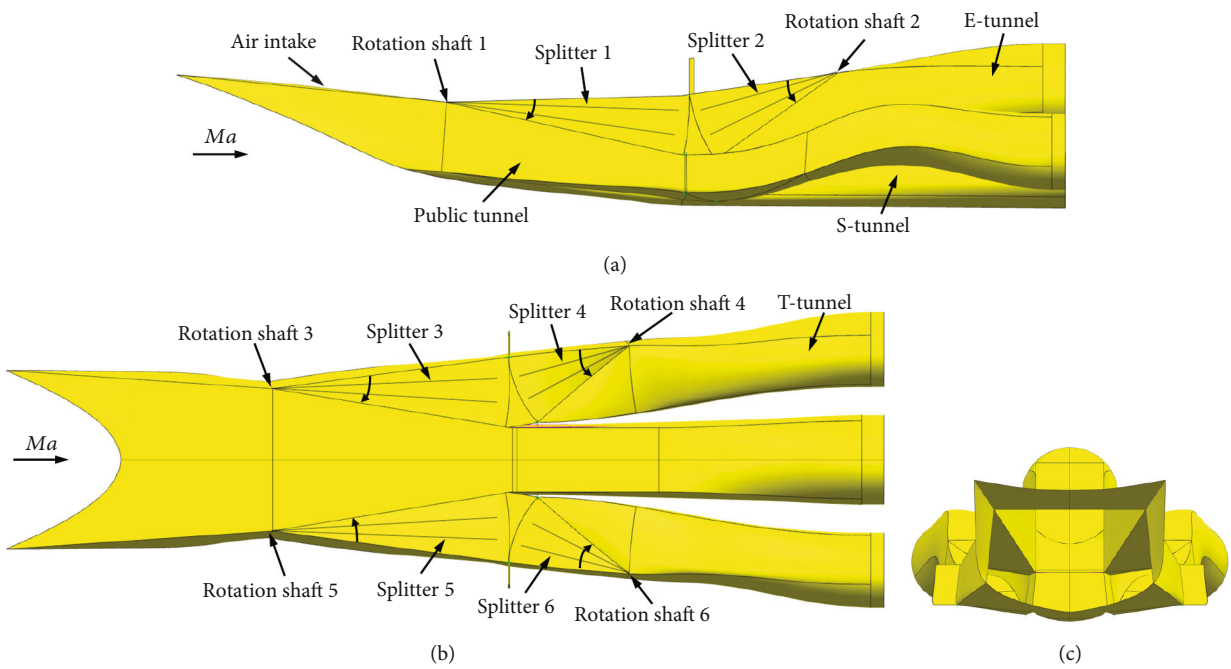

Figure 1: Schematic geometric diagram of the hypersonic combined inlet: (a) front view; (b) vertical view; (c) end view.

not only predict the inlet unstart but also reflect the degree of instability and provides a range of unstart margins for advance control

(2) Combined with machine learning techniques, a critical backpressure ratio prediction method for inlet start/unstart state is introduced. This approach can effectively reveal exactly how much backpressure ratio the inlet becomes unstart, which is used as the critical condition to predict the unstart state

(3) By extracting the optimal surface pressure measurement points along the inlet ducts, a 1D-CNN is utilized to construct surface pressure-backpressure prediction models for each engine mode. In this paper, the model predictions are validated using experimental data, demonstrating the effectiveness of the proposed approach

The rest of the paper is organized as follows: Section 2 briefly describes the hypersonic combined inlet model and the CFD dataset from numerical simulations. Section 3 specifically introduces the inlet unstart prediction and warning method and its realization processes. Section 4 presents the relevant results of the proposed method and performs the experimental validation. Finally, Section 5 gives some conclusions.

2. Inlet Model and CFD Dataset

2.1. Combined Inlet Model. The three-dimensional inward-turning multiducted combined inlet was proposed by Zhu et al. [37, 38]. Cai et al. [39] confirmed that its geometric aerodynamic characteristics can meet the requirements of the propulsion system, which is capable of continuous operation in a wide speed range. The schematic geometric diagram of the inlet is shown in Figure 1. The two side tunnels represented by T are the flow ducts for the turbine engine, the lower tunnel represented by E is the flow duct for the ejector ramjet engine, and the upper tunnel represented by S is the flow duct for the scramjet engine. Additionally, the splitter plates are arranged in the twin-turbine ducts and ejector ramjet duct, and the mode transition from turbine mode to ejector ramjet mode and from ejector ramjet mode to scramjet mode can be completed by rotating splitters along corresponding rotation shafts.

2.2. Numerical Method. The numerical simulations are performed using the ANSYS FLUENT 14.5 software. Density-based 3D Reynolds-Averaged Navier-Stokes (RANS) equations are solved with the two-equation k-ω shear stress transport (SST) turbulence model. The flux term is solved using the Roe-FDS (Roe flux-difference splitting) difference scheme. The first-order upwind scheme is used to discretize the equations spatially to get a stable initial flow field, based on which the second-order upwind scheme is further applied for a refined resolution. Convergence criteria for the calculations are determined by at least three orders of magnitude reduction in the residuals of the continuity equation, momentum equation, energy equation, and k-ω equation, as well as a stable flow rate at the inlet and outlet sections. The characteristic index remains relatively unchanged throughout the iterative process. Assuming that the fluid is an ideal gas, the constant pressure specific heat is fitted by piecewise polynomial, and the viscosity is solved by the Sutherland formula. Various boundary conditions are used during the calculations, including the pressure far-field boundary, pressure outlet boundary, nonslip adiabatic solid wall boundary, and symmetry boundary. The windward

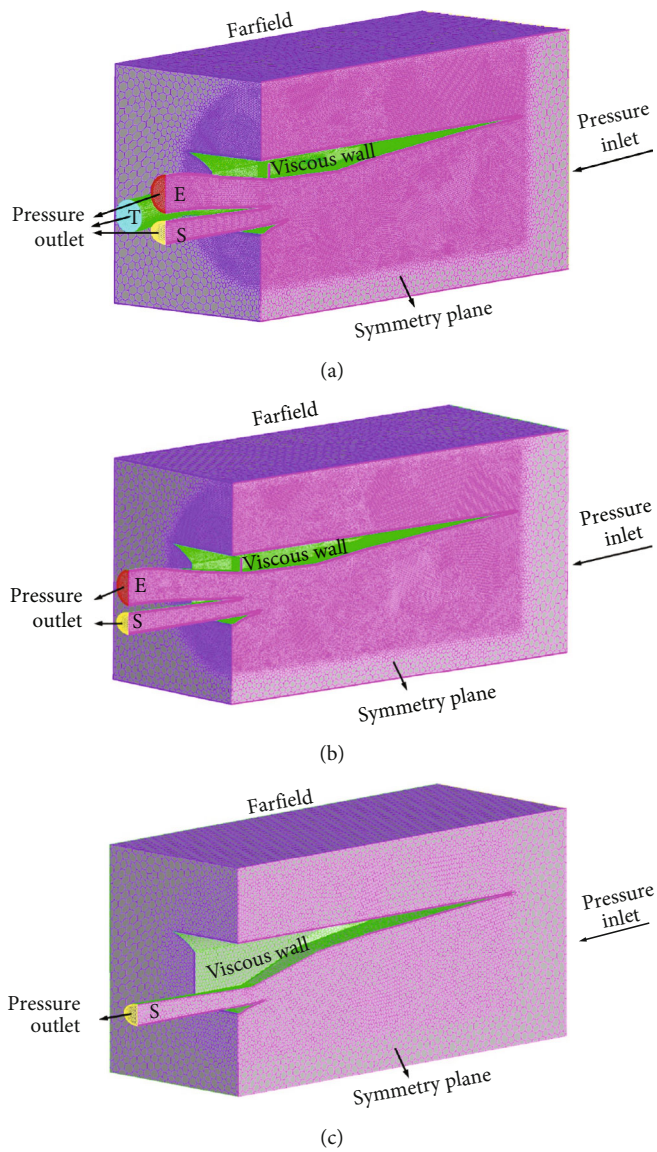

Figure 2: Calculation grid for each mode: (a) TUR mode with 8×10^6 cells; (b) ERJ mode with 6×10^6 cells; (c) SCR mode with 4×10^6 cells.

side of the incoming flow is considered the pressure far field, the outlet section of each channel is set as the pressure outlet, and the wall surface adopts the adiabatic nonslip boundary condition, regardless of heat transfer.

To meet the requirements of different Mach number computational domain scales and consider the tunnel regulation conditions of the combined inlet, this paper involves three sets of computational grids, including one set for turbine mode, one set for ejector mode, and one set for scramjet mode. Only half of the inlet model is used for simulation in consideration of its symmetric configuration. Each mesh set adjacent to the wall is refined to ensure $y^+ < 30$ to capture the surface boundary layer accurately, as shown in Figure 2. Table 1 summarizes the freestream conditions, engine modes, and mesh quantities of the calculation conditions in this work.

To verify the reliability of the calculation results, the grid-independent verification of the typical working condition of Mach number 5.0 is carried out. By comparing the results of coarse mesh (2 million), medium mesh (4 million), and fine mesh (6 million) shown in Figure 3, it is observed that the pressure distribution is basically the same for different numbers of meshes, indicating that the mesh factor does not affect the numerical calculation in this paper. Taking into account the convergence and computational efficiency of mesh grids, the medium grid with a total cell number of 4 million is chosen to carry out the research and analysis. For other calculation states, the grid quantity is referred to the working condition and adjusted accordingly based on the calculation domain and the number of tunnels.

Additionally, to validate the effectiveness of the turbulence model chosen in reflecting the flow characteristics inside the inlet, as well as to ensure the reasonableness of the numerical simulation boundary condition settings. The experimental model [40] is simulated using the numerical method illustrated in Figure 4, with the incoming flow

Table 1: The working conditions of numerical cases.

Ma	H (km)	Mode	Mesh (1×10^6)	Backpressure ratios
1.5	9.1	TUR	8	1, 1.2, 1.4, 1.8, 2, 2.2, 2.4, 2.6
2.0	13	TUR	8	1, 1.5, 2, 2.5, 3, 3.5, 4.25, 4.5, 4.75, 5
2.5	15.5	TUR	8	1, 2, 3, 4, 6, 7, 8, 9
2.5	15.5	ERJ	6	1, 4, 6, 7, 8
3.0	18.5	ERJ	6	1, 2, 4, 5, 6, 7, 8.5, 9.5, 11
4.0	22.7	ERJ	6	1, 3, 6, 9, 12, 15, 16, 17, 18
4.0	22.7	SCR	4	1, 5, 10, 20, 30, 40, 50
4.5	24	SCR	4	1, 10, 20, 30, 40, 50, 60, 70, 80
5.0	26	SCR	4	1, 10, 20, 30, 40, 60, 80, 90, 100, 110, 115
6.0	28	SCR	4	1, 10, 20, 40, 70, 80, 90, 95, 110, 120, 125, 130, 135

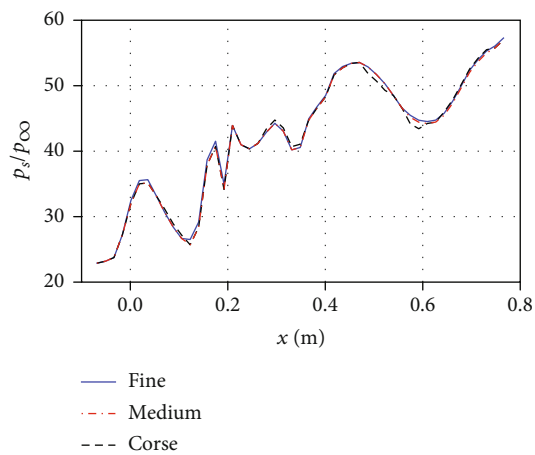

Figure 3: Calculation results of different mesh qualities.

conditions referenced to Ref. [40]. Figure 5 presents the comparison of the pressure distribution between the experiment and simulation. The simulation results demonstrate good agreement with the experimental results in terms of both numerical values and curve trends, further verifying the accuracy of the numerical method employed.

2.3. CFD Dataset. For the typical working points (noted as TUR#1~TUR#3, ERJ#1~ERJ#3, and SCR#1~SCR#4) selected in Table 1, simulation states of each working point under different backpressure ratios are also provided. The maximum backpressure ratio of each working point in the table corresponds to the unstart state of the inlet, and the rest corresponds to the unstart states. The backpressure ratio is defined as follows:

$$p_r = \frac{p_b}{p_\infty}, \tag{1}$$

where p_b represents the backpressure at the exit of the isolator and p_∞ represents the static pressure of the freestream. Figure 6 indicates the pressure monitoring points on the surface lines of each inlet duct to obtain the CFD dataset through numerical simulation. Due to the symmetrical geometry of the combined inlet, only half of the surface pressure monitoring points are set for each duct. In this case, 100 measurement points are averagely set for each surface line, corresponding to one surface pressure sample data. These samples under all surface lines are used to compose the CFD dataset at each p_r, where the surface pressure coefficient is derived from the dimensionless conversion of the surface pressure, defined as follows:

$$C_p = \frac{p_s}{p_\infty}, \tag{2}$$

where p_s represents the surface pressure. By constructing the prediction models between the surface pressure coefficient C_p and the backpressure ratio p_r for each engine mode, this study attempts to reflect the backpressure at the exit of the isolator through the surface pressure for applying to the inlet unstart prediction and warning.

3. Backpressure Unstart Prediction and Warning Method

The method consists of the following steps: (1) the determination of the inlet unstart and unstart warning boundary of surface pressure at typical working points, (2) the construction of critical backpressure conditions for wide speed range, (3) the establishment of the backpressure prediction models for each engine mode, and (4) the realization of unstart prediction and warning.

Figure 7 shows the analytical process of the main work of the inlet unstart prediction and warning. Process (I) is the classification of the inlet start/unstart state based on 10-CV SVM, which is used for solving the unstart boundary of surface pressure. Where an unstart margin η is set to determine the unstart warning boundary for surface pressure, the data information (represented by support vectors) on the boundaries is used as the regression inputs for the prediction of the critical backpressure ratios. Process (II) is the regression prediction and wide speed range fitting of the critical backpressure ratios. The regression models for p_r are trained by the

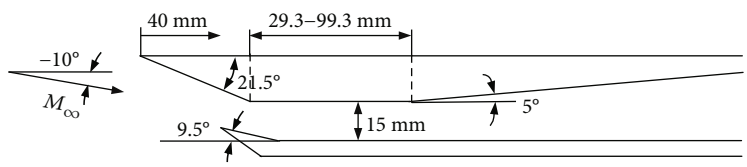

Figure 4: Experimental model used in ref. [40].

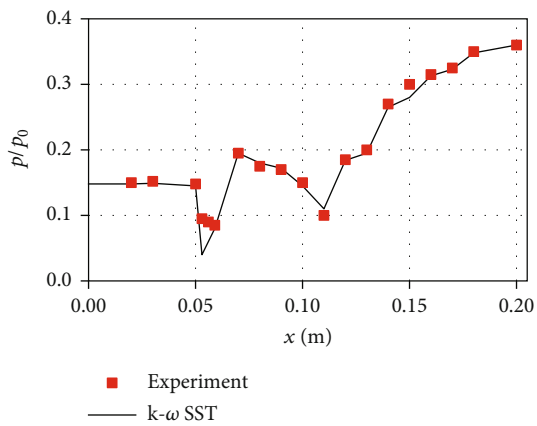

Figure 5: Streamwise variation of surface pressure.

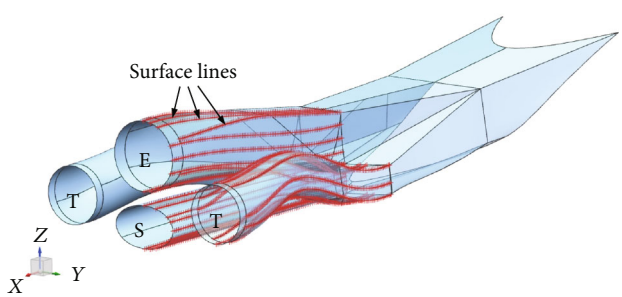

Figure 6: The surface pressure monitoring points along the inlet ducts.

BP neural network to predict p_u and p_{uw} at typical working points. These prediction results will be used to fit the three-dimensional curves of (Ma, H, p_u) and (Ma, H, p_{uw}) for each engine mode. Process (III) is the establishment of the C_p-p_r prediction models. It adopts the 1D-CNN to establish the C_p-p_r prediction models between the surface pressure coefficient and the backpressure ratio for each engine mode based on the determination of the optimal surface pressure measurement points. Process (IV) is the realization of the unstart and unstart warning state detection of the inlet. The data of the inlet for the optimal measurement points on one surface line is taken and then dimensionless and normalized. Support p_r^* as the prediction result obtained from the C_p-p_r prediction models, while p_u^* and p_{uw}^* are the fitting values of (Ma, H, p_u) and (Ma, H, p_{uw}) curves under the flight freestream condition. By comparing the result of p_r^* with p_u^* and p_{uw}^*, the current state of the inlet (start state, unstart warning state, and unstart state) can be detected.

3.1. Inlet Unstart Boundary and Unstart Warning Boundary of Surface Pressure. Chang et al. [33–35] studied the start/unstart state classification of inlet surface pressure data and proposed the boundaries of inlet start and unstart based on the SVM classification criterion. However, since the classification is only for current pressure data, this study adopts the 10-fold cross-validation approach to find the optimal hyperplane of SVM and enhance its generalization ability to accommodate more samples. In this paper, the optimal hyperplane that divides the start and unstart states of the inlet is called the inlet unstart boundary of surface pressure, which is expressed as follows:

$$\sum_{i=0}^{m} \omega_i x_i + b = 0, \tag{3}$$

where ω_i and b represent the ith weight and the bias of the optimal hyperplane of SVM with a linear kernel, respectively, x_i represents the ith feature corresponding to the surface pressure, and m is the number of features of the samples. To be applied to the unstart warning of the inlet, this paper determines the inlet unstart warning boundary of surface pressure by setting the unstart margin η based on the unstart boundary of surface pressure, which is expressed as follows:

$$\sum_{i=0}^{m} \omega_i (x_i + \eta) + b = 0. \tag{4}$$

From Eqs. (3) and (4), the unstart boundary and unstart warning boundary of surface pressure kept the η apart at each axial direction in the pressure feature space. However, it is difficult to express the surface pressure distribution of the inlet under critical states through the unstart boundary and the unstart warning boundary. The support vectors of SVM play a crucial role in this regard, as they maintain a maximum soft interval in the sample space and are equidistant from the optimal classification boundary [41]. The inlet unstart boundary is determined by the support vectors of the positive class (start) and negative class (unstart). Therefore, the surface pressure coefficient data information at the boundaries can be represented by the positive and negative support vectors and the positive and negative support vectors at unstart margin, respectively, as shown in Figure 8, where

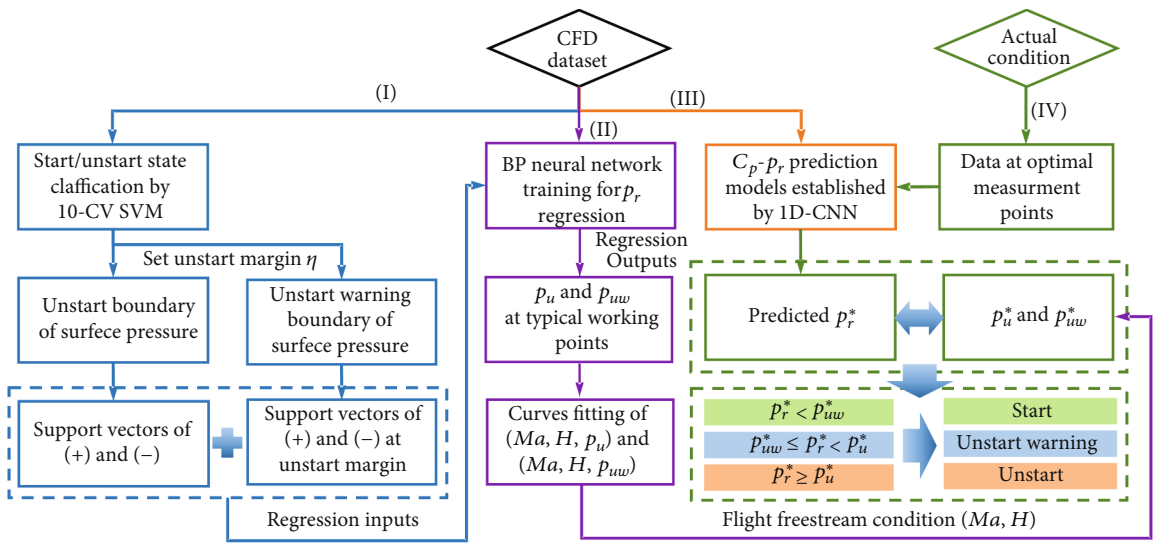

Figure 7: Specific processes of inlet unstart prediction and warning method.

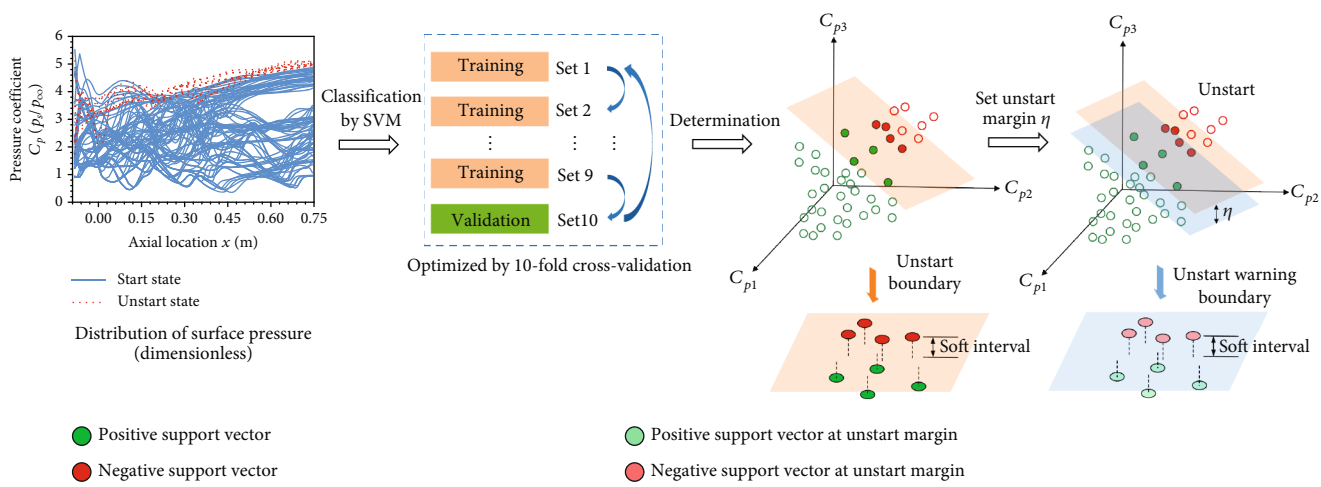

Figure 8: The determination process of the unstart and unstart warning boundary of surface pressure.

$C_{p1} \sim C_{p3}$ represents the three different features of surface pressure coefficient, taking the three-dimensional feature space as an example.

3.2. The Construction of Critical Backpressure Conditions for Wide Speed Range. In some numerical simulations [15, 32–34] with different backpressures for inlet models, high backpressure can trigger the inlet flow field unstable, resulting in the unstart occurring. Figure 9 shows the flow evolution (Mach number distribution) at the combined inlet when the backpressure changes from $p_r = 1$ to $p_r = 5$ at Mach 2 in the simulations. As the backpressure increases, the boundary layer thickens, and the thickened boundary layer generates a strong induced shock wave. This, in turn, promotes boundary layer delamination, forming an unstart shock wave. As this interaction progresses, the delamination bubble at the top of the containment meets the boundary layer pushing in from the rear, causing a significant reduction in mass inflow and finally inlet unstarting.

Meanwhile, in Section 3.1, the negative class support vectors (partial unstart samples of surface pressure) of the unstart boundary in Figure 8 are included in the unstable flow field at $p_r = 5$ of the figure conversely, and the positive class support vectors (partial start samples of surface pressure) correspond to the stable flow field cases at other p_r states. Although different backpressure ratios can be simulated to reflect the process of the inlet from start to unstart, the exact values of the backpressure ratio cannot be known when the inlet starts unstart and unstart warning. To address this issue, this study establishes the regression models of backpressure ratio using the BP neural network to predict them based on the inputs provided in Section 3.1.

Here, the input and output are normalized separately during data training process. For data division, a certain proportion of samples are randomly selected for data training by the BP neural network with Adam optimizer, and the remaining 20 samples are used for testing. The neural network adopts a "100-20-1" topology in which the hidden

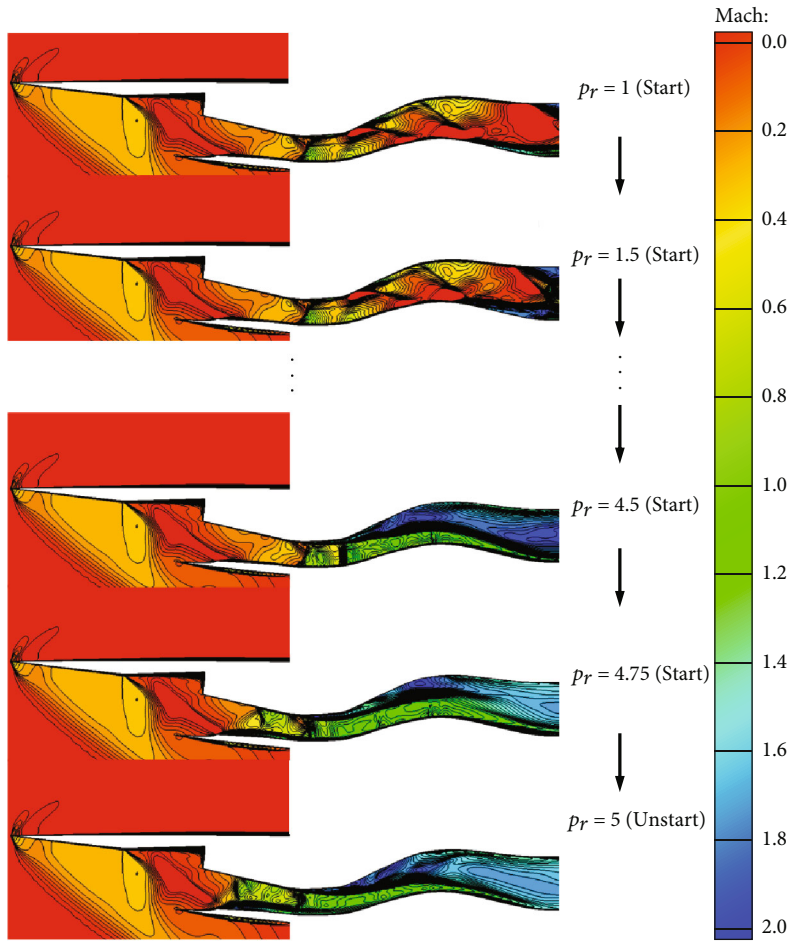

Figure 9: Mach number contours at the combined inlet of the process from start to unstart at Mach 2.

layer uses the rectified linear unit (ReLU) activation function and the output layer uses the linear function, as shown in Figure 10, where $\{C_{p1}, C_{p2}, \cdots, C_{p100}\}$ represents all the scaled surface pressure coefficient inputs of the neural network and $\widehat{p}_r$ represents the predicted backpressure ratio obtained by inverse scaled operation on the output. Define the mean squared error (MSE) between the p_r and $\widehat{p}_r$ as the loss function of the network, as shown in the following equation:

$$\text{Loss} = \text{MSE}(p_r, \widehat{p}_r) = \frac{1}{N}\sum_{i=1}^{N}\left(p_{r(i)} - \widehat{p}_{r(i)}\right)^2, \tag{5}$$

where N is the number of the training/test set sample, $p_{r(i)}$ represents the actual backpressure ratio of the ith sample, and $\widehat{p}_{r(i)}$ represents the predicted backpressure ratio of the ith sample. By adjusting the learning rate α and the decay rate γ of the learning rate of the optimizer, ensure that the training loss and test loss converge before 2000 iterations during the training process, which can obtain the optimal regression models of each working point. Finally, these models are used to predict the inlet critical backpressure ratios p_u and p_{uw} for each working point.

Where concerning the regression inputs of the critical backpressure ratios, the support vectors of SVM are equidistant from the optimal hyperplane (unstart boundary). We can give the positive and negative support vectors $V = \{v_1^+, v_2^+, \cdots, v_m^+; v_1^-, v_2^-, \cdots, v_n^-\}$ of SVM and the positive and negative support vectors at unstart margin denoted by $W = \{w_1^+, w_2^+, \cdots, w_m^+; w_1^-, w_2^-, \cdots, w_n^-\}$. The prediction of the critical backpressure ratios is calculated by the following formulas:

$$p_u = \frac{1}{2}\left[\frac{p(v_1^+) + p(v_2^+) + \cdots + p(v_{\mathrm{m}}^+)}{m} + \frac{p(v_1^-) + p(v_2^-) + \cdots + p(v_n^-)}{n}\right], \tag{6}$$

$$p_{uw} = \frac{1}{2}\left[\frac{p(w_1^+) + p(w_2^+) + \cdots + p(w_m^+)}{m} + \frac{p(w_1^-) + p(w_2^-) + \cdots + p(w_n^-)}{n}\right], \tag{7}$$

where $\{p(v_1^+), p(v_2^+), \cdots, p(v_m^+)\}$ and $\{p(v_1^-), p(v_2^-), \cdots, p(v_n^-)\}$ represent the prediction results of V and $\{p(w_1^+), p(w_2^+), \cdots, p(w_m^+)\}$ and $\{p(w_1^-), p(w_2^-), \cdots, p(w_n^-)\}$ represent the prediction results of W. The value of p_u is calculated from the average of $[p(v_1^+) + p(v_2^+) + \cdots + p(v_m^+)]/m$ and $[p(v_1^-) + p(v_2^-) + \cdots + p(v_n^-)]/n$ which represent the average prediction results of the scaled pressure of positive and negative class support

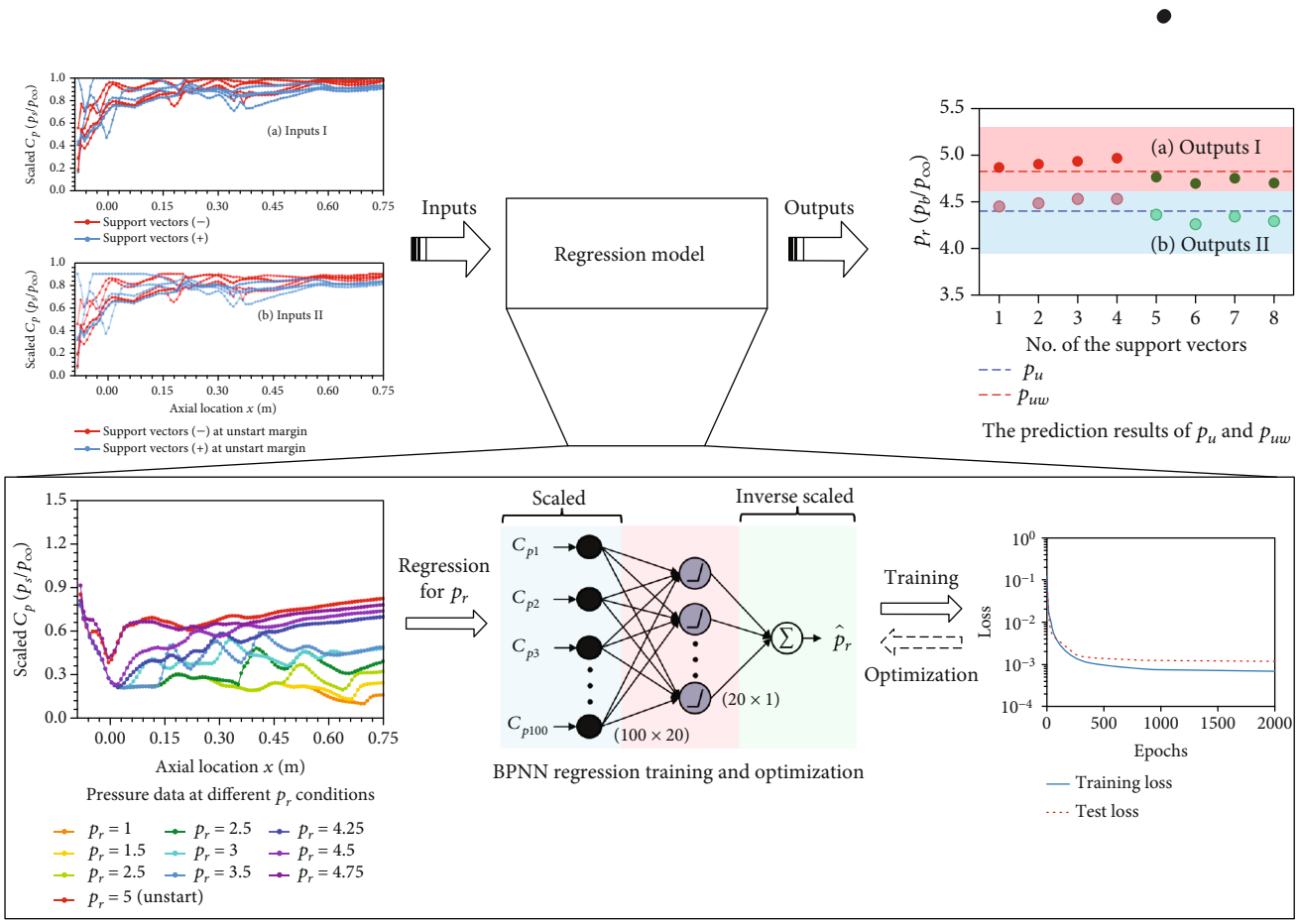

FIGURE 10: The prediction process of the critical backpressure ratios based on regression model.

vectors, respectively, and the calculation process of the value of p_{uw} is likewise as it.

The critical backpressure ratios of each working point are only applicable to the unstart prediction and warning of discrete typical working states. To apply for other working points in the wide speed range, it is necessary to construct the relationship between the Mach number, height, and the critical backpressure ratios p_u and p_{uw} by curve fitting. The flight Mach number and height at other working points can be solved by interpolation method and then fitted to the three-dimensional curves of (Ma, H, p_u) and (Ma, H, p_{uw}), which is done by the least squares polynomial fitting way with the following equations:

$$p_u^* = C_0 + C_1\mathrm{Ma} + C_2H + C_3\mathrm{Ma}\cdot H + C_4\mathrm{Ma}^2 + C_5H^2, \quad (8)$$

$$p_{uw}^* = C_7 + C_8\mathrm{Ma} + C_9H + C_{10}\mathrm{Ma}\cdot H + C_{11}\mathrm{Ma}^2 + C_{12}H^2, \quad (9)$$

where $C_0 \sim C_{11}$ are constant terms and the p_u^* and p_{uw}^* on the fitting curves can be directly expressed by the freestream conditions (Ma and H).

3.3. Establishment of the C_p-p_r Prediction Models for Each Engine Mode. In the unstart prediction and warning, to obtain the current backpressure ratio of the inlet through the surface pressure data, it is critical to establish the backpressure ratio prediction models for each engine mode. The C_p-p_r prediction models are constructed by 1D-CNN with the surface pressure coefficient as input and the corresponding backpressure ratio as output. Also, to improve the utility of the surface pressure measurement points, only a few optimal measurement points are considered for the input to connect the model for training. The training process of the models simultaneously ensures that all data is scaled to the range of (0, 1) and the model output is eventually inversely normalized. It adopts 1 upsampling layer, 3 convolutional layers with the ReLU activation function, 2 maxpooling layers, and 1 fully connected layer with the linear function, as shown in Figure 11.

The data extraction for optimal measurement points adopts the regression feature selection method. Generally, numerous studies [32–34] on the feature selection of surface pressure monitoring points of the inlet are dedicated to solve the problems of start/unstart state classification. However, for the backpressure prediction at the exit of the isolator, this study implements the SVR-RFE algorithm for regression feature selection, to extract several significant surface pressure measurement points of the inlet to monitor the backpressure. It is worth noting that after feature selection, the

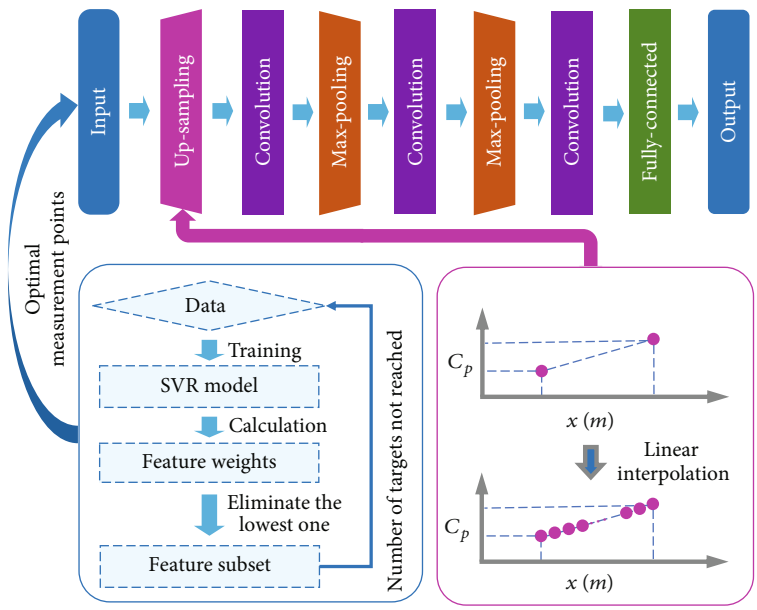

Figure 11: The C_p-p_r prediction model based on the feature selection and upsampling operations.

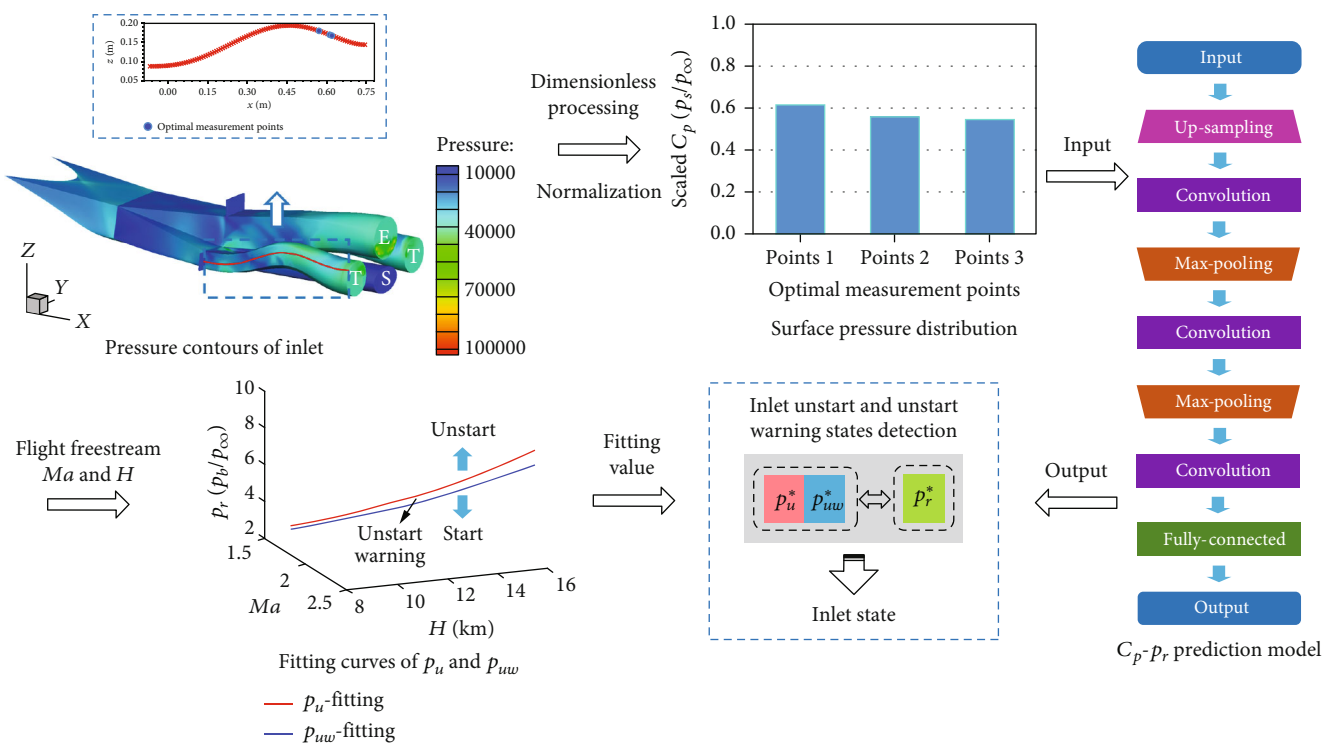

Figure 12: The process of realization for the inlet unstart and unstart warning state detection.

Table 2: The results of surface pressure classification for each working point.

Working points	TUR #1	TUR #2	TUR #3	ERJ #1	ERJ #2	ERJ #3	SCR #1	SCR #2	SCR #3	SCR #4
Classification accuracy	100%	100%	100%	100%	100%	100%	100%	100%	100%	100%
No. of positive support vectors	3	4	3	3	4	4	3	4	6	6
No. of negative support vectors	5	5	3	2	3	3	4	3	3	4

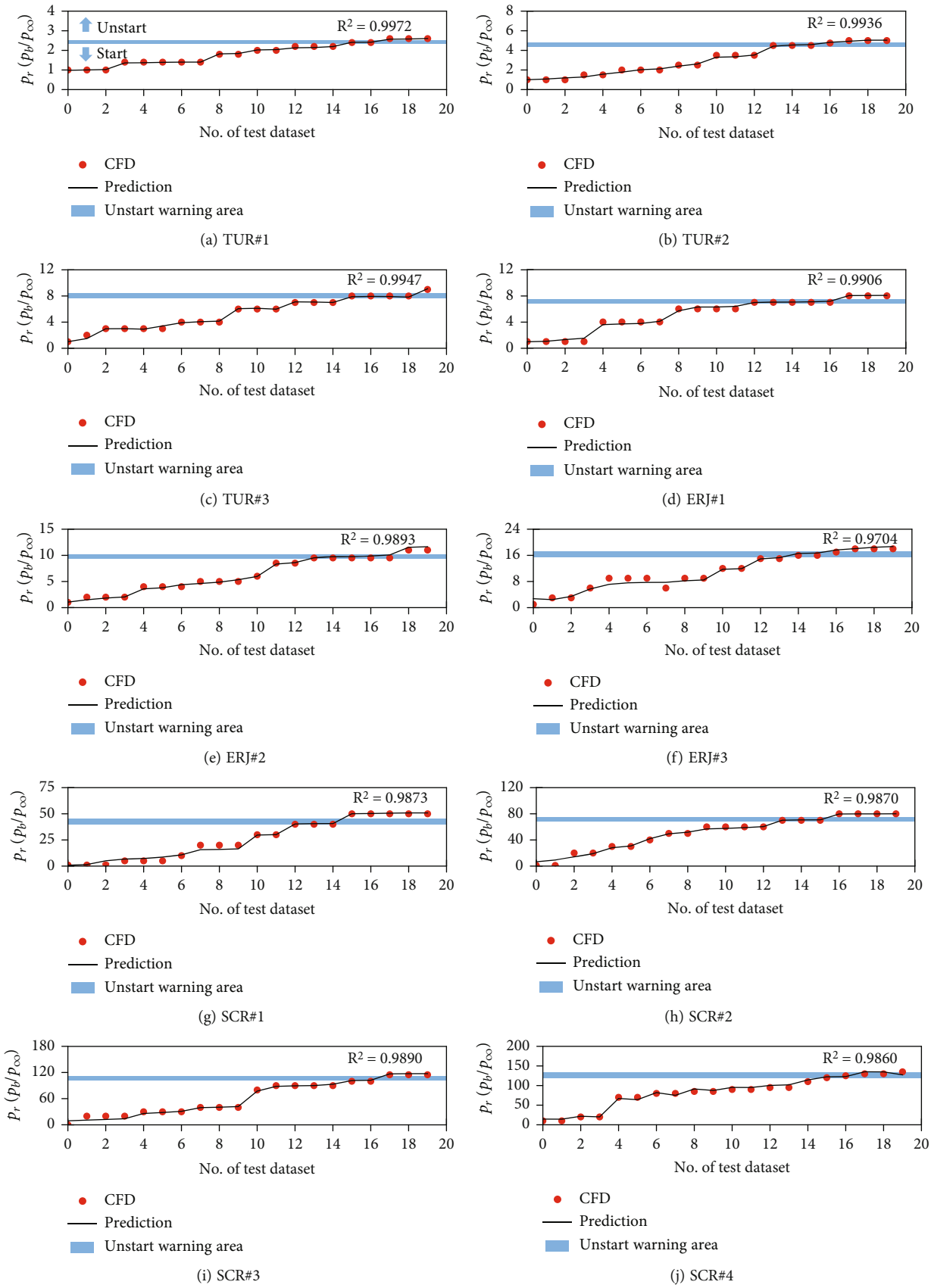

Figure 13: Comparison between the predictions and the CFD results on the test dataset for typical working points from (a) TUR#1 to (j) SCR#4.

Table 3: The prediction results of critical backpressure ratios at typical working points.

Working points	TUR #1	TUR #2	TUR #3	ERJ #1	ERJ #2	ERJ #3	SCR #1	SCR #2	SCR #3	SCR #4
p_u	2.496	4.825	8.468	7.514	10.159	17.211	45.111	75.225	112.891	132.290
p_{uw}	2.335	4.384	7.693	6.892	9.359	15.489	39.841	68.752	102.498	118.485

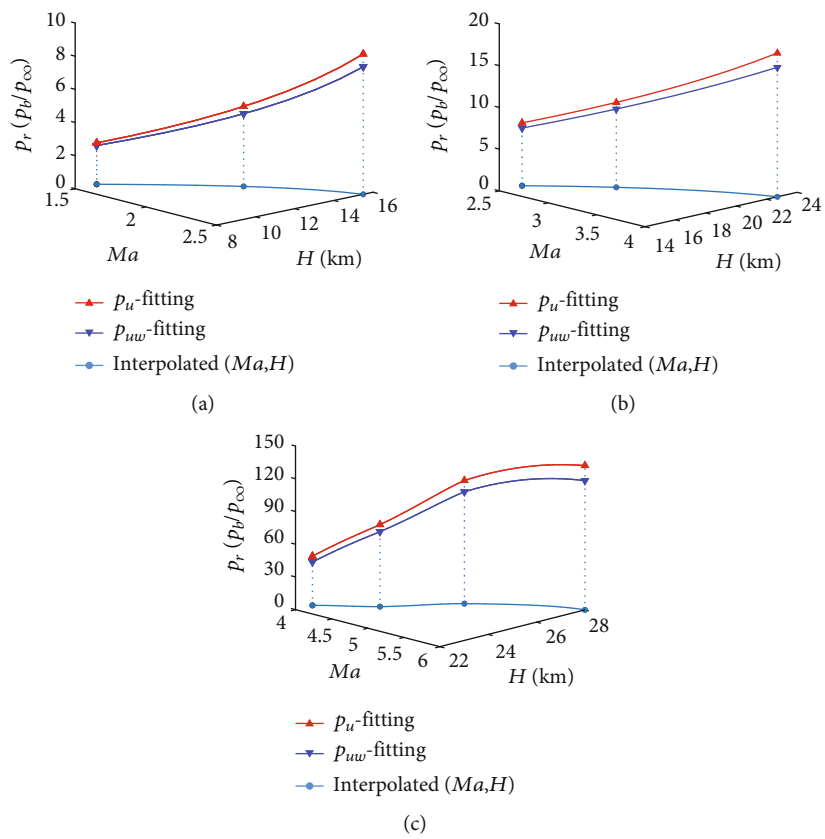

Figure 14: The fitting curves of the p_u and p_{uw} for each engine mode: (a) TUR mode; (b) ERJ mode; (c) SCR mode.

dimensionality of the pressure data gets greatly reduced, making it necessary to enlarge the data size by upsampling. Linear interpolation as a common upsampling method can be used to expand the surface pressure dimension to connect the convolutional neural network for data training.

Considering the actual backpressure scenario of the combined engine operation, the dataset without the through-flow state ($p_r = 1$) presented in Table 1 is selected for each working point. In the model evaluation, the mean absolute percentage error (MAPE) and the correlation coefficient (R^2) are employed, defined as follows:

$$\mathrm{MAPE}(p_r, p_r^*) = \frac{1}{n}\sum_{i=1}^{n}\frac{\left|p_{r(i)} - p_{r\,(i)}^*\right|}{p_{r(i)}} \times 100\%, \tag{10}$$

$$R^2(p_r, p_r^*) = 1 - \frac{\sum_{i=1}^{n}\left(p_{r(i)} - p_{r\,(i)}^*\right)^2}{\sum_{i=1}^{n}\left(p_{r(i)} - p_r\right)^2}, \tag{11}$$

where n is the number of the validation set sample; $p_{r(i)}$ and $p_{r\,(i)}^*$ represent the actual and predictive backpressure ratio of the ith sample, respectively; and p_r represents the mean value of the predicted backpressure ratio of the validation set sample.

3.4. Method for Inlet Unstart and Unstart Warning State Detection. The unstart prediction and warning method is mainly based on the three-dimensional fitting curves of (Ma, H, p_u) and (Ma, H, p_{uw}), and the C_p-p_r prediction models, where the implementation process of the method is shown in Figure 12.

The inlet pressure data is taken at optimal measurement points on the one surface line of the tunnel under the current engine operating condition, adopting dimensionless processing (divided by the static pressure of the freestream) into the pressure coefficient as well as normalized. Then, the value of p_r^* at the exit of the isolator can be predicted by the C_p-p_r prediction models. For the current flight freestream condition (Ma and H), the values of p_u^* and p_{uw}^* can be obtained from the fitting curves of critical backpressure

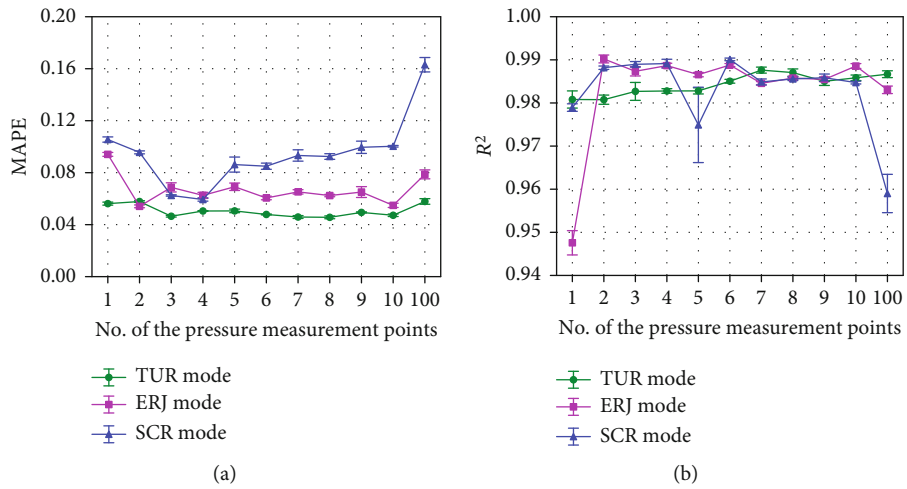

Figure 15: The evaluation results for each engine mode with the selected number of measurement points: (a) MAPE results on the validation set; (b) R^2 results on the validation set. The error bars represent the standard deviation of the validation results of the trained models for five runs.

ratios. The inlet state can be reflected by the comparison between the current predicted backpressure ratio p_r^* and the critical conditions p_u^* and p_{uw}^*, completing the unstart and unstart warning state detection. Equation (12) can be used as the detection judgment of the inlet state, where "1" represents the start state, "0" represents the unstart warning state, and "−1" represents the unstart state, defined as follows:

$$S_{\text{inlet}} = \begin{cases} 1, p_r^* < p_{uw}^* \\ 0, p_{uw}^* \le p_r^* < p_u^* \\ -1, p_r^* \ge p_u^*. \end{cases} \tag{12}$$

4. Results and Discussion

4.1. The Start/Unstart Classification Results of Inlet Surface Pressure. The SVM training is optimized by 10-fold cross-validation to determine the optimal hyperplane, where the accuracy of the surface pressure classification is 100% for each working point, as shown in Table 2. The number of the positive (start class) and negative (unstart class) support vectors based on all the surface pressure features at each working point is also counted. These support vectors and the support vectors at unstart margin represent the data information at the unstart boundary and unstart warning boundary of surface pressure, respectively, which are used as the regression inputs for the critical backpressure ratios p_u and p_{uw}. In this paper, the unstart margin is considered as a constant value to address the inlet unstart warning problem. To not cross the unstart boundary, it is essential to set a reasonable unstart margin to determine the unstart warning boundary, such as 10% in this study.

4.2. The Results of Prediction and Wide Speed Range Fitting for Critical Backpressure Ratios. The purpose of the critical backpressure ratios prediction is to determine the backpressure ratios for the unstart and unstart warning states of the inlet through the surface pressure data. Referring to the training process of regression models in Figure 5, for the samples of the typical working points at each engine mode, a certain percentage of samples are randomly selected for training and the remaining 20 samples for testing. The hyperparameters α and γ are adjusted for optimization based on the convergence of the training and test loss curve of the BP neural network.

Table 4: The results of the optimal measurement points for each engine mode.

Engine mode	Combination of measurement points	MAPE	R^2
TUR	[77, 82, 83]	0.0465	0.9827
ERJ	[81, 99]	0.0541	0.9902
SCR	[90, 91, 98, 99]	0.0594	0.9891

The comparison between the predicted backpressure ratio results by the BP neural network regression models and the CFD results on the test dataset is shown in Figure 13. The blue area marked in the figure is the unstart warning area at the working points, containing the 10% unstart margin of surface pressure. The upper part is the unstart backpressure ratio area, and the lower part is the start backpressure ratio area. Therefore, the backpressure ratio can represent the state of the inlet. The average result of the correlation coefficient R^2 referring to the definition in Eq. (11) for all working points in Figures 13(a)–13(j) is 0.9885. It indicates that the prediction results of regression models on the test dataset agree well with the CFD values, especially in the high backpressure state parts.

Combined with the number of regression inputs determined for each working point shown in Table 2, refer to the regression prediction process of the critical backpressure ratios shown in Figure 10 and the calculation of Eqs. (6) and

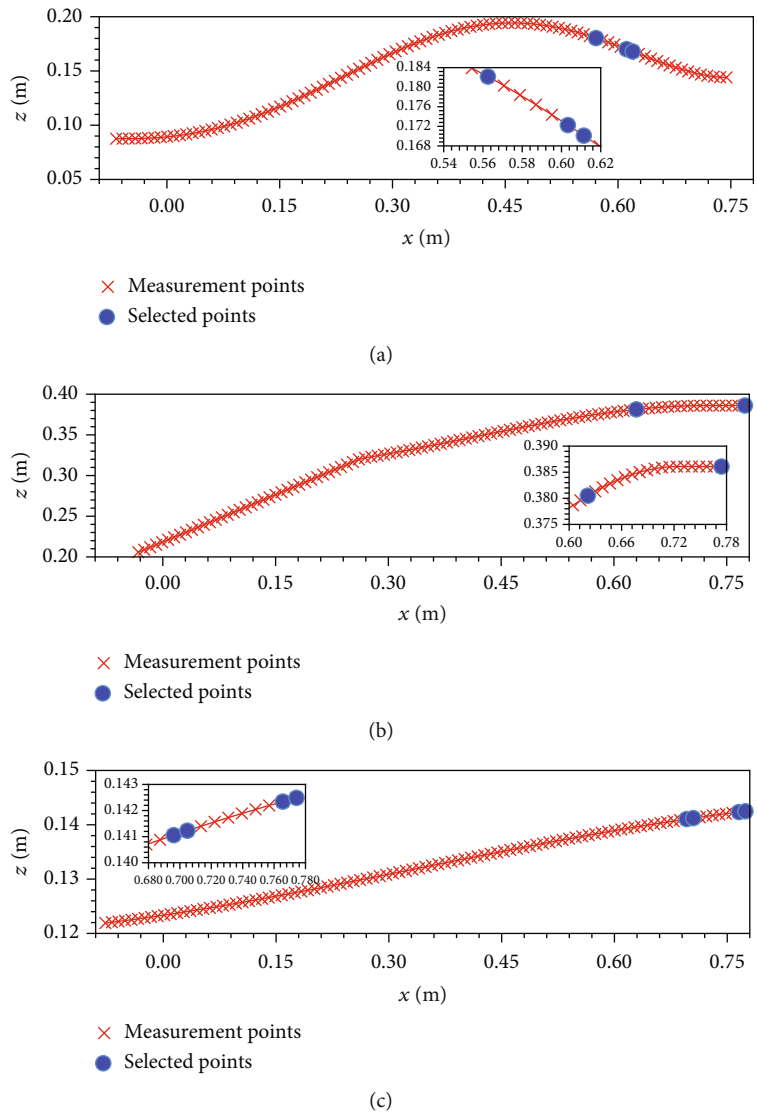

Figure 16: The marked optimal measurement points at surface lines for (a) TUR mode, (b) ERJ mode, and (c) SCR mode.

(7) of the critical backpressure ratios. The average prediction results of the p_u and p_{uw} based on 20 runs at each working point are shown in Table 3. It can be found that the predicted values of the p_u are between the backpressure ratio of the unstart state and the maximum backpressure ratio of the start state shown in Table 1, indicating that the prediction of the critical backpressure ratios is consistent with reality.

For the freestream conditions from Table 1, the Mach number and height are interpolated by the segmented cubic Hermite method [42]. Based on the prediction results of the critical backpressure ratios in Table 3, Eqs. (9) and (10) are used to fit the three-dimensional curves of (Ma, H, p_u) and (Ma, H, p_{uw}) within the interpolated (Ma, H) for each engine mode, as shown in Figure 14. This allows that the critical backpressure ratios at other working points can be determined approximately.

4.3. The Performance of C_p-p_r Prediction Models. The surface pressure measurement point selection for each engine mode is implemented by the SVR-RFE algorithm. To investigate the effect of model accuracy on the number of selected measurement points, model validation evaluations based on 1 to 10 measurement points are carried out, while the comparison of all measurement points is performed. The dataset is divided into the 80% training set and 20% validation set where the validation is performed five times through the trained model, and the results are shown in Figure 15.

It can be observed that the validation results of MAPE and R^2 decrease initially and then increase later with the increase of the selected measurement points. The validation errors are minimized when 3, 2, and 4 measurement points are selected for the TUR, ERJ, and SCR modes, respectively. As shown in Table 4, the MAPE for these modes is as low as around 5%, and the corresponding R^2 reaches above 0.98. Compared with 100 measurement points, it can reduce most of the surface pressure measurement points and improve the prediction accuracy of the model to some extent.

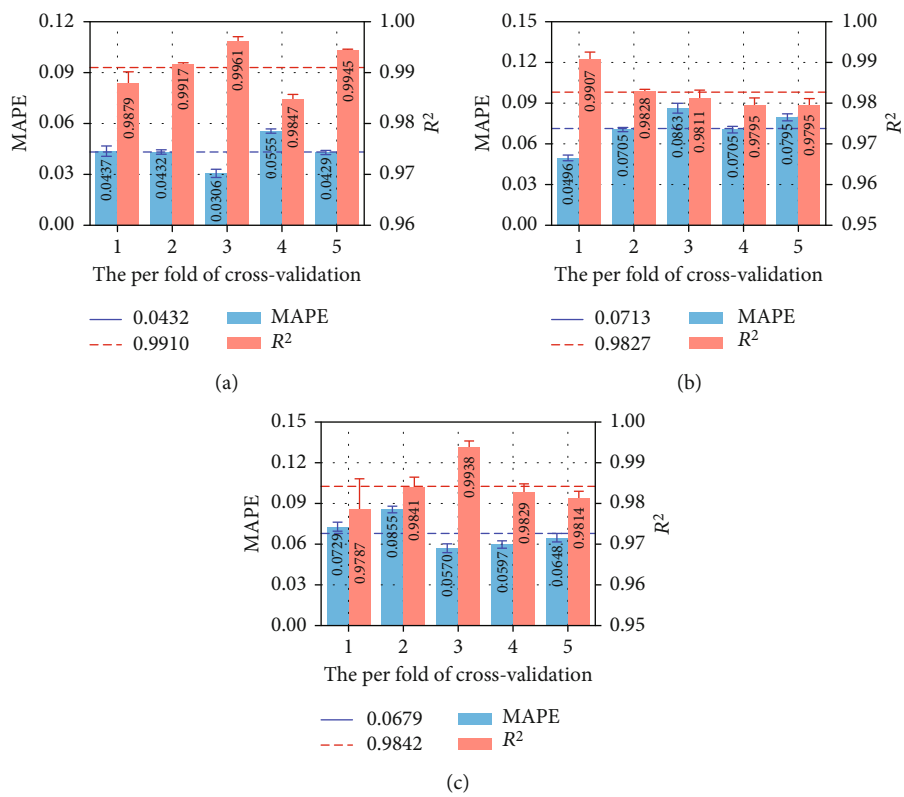

Figure 17: The evaluation results of the C_p-p_r prediction models based on 5-fold cross-validation: (a) TUR mode; (b) ERJ mode; (c) SCR mode. The error bars represent the standard deviation of models' evaluation results on cross-validation for five runs.

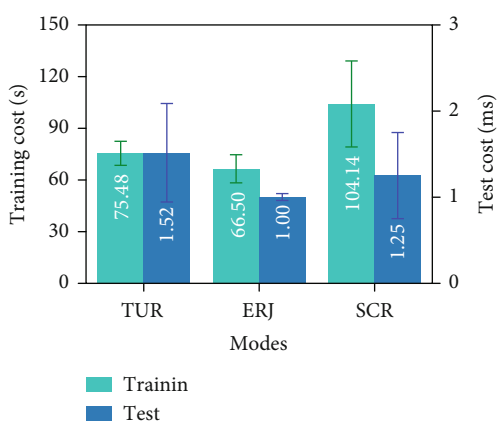

Figure 18: The time cost for each C_p-$p_r$prediction models. The error bars represent the standard deviation of models' training/test time costs for 10 runs.

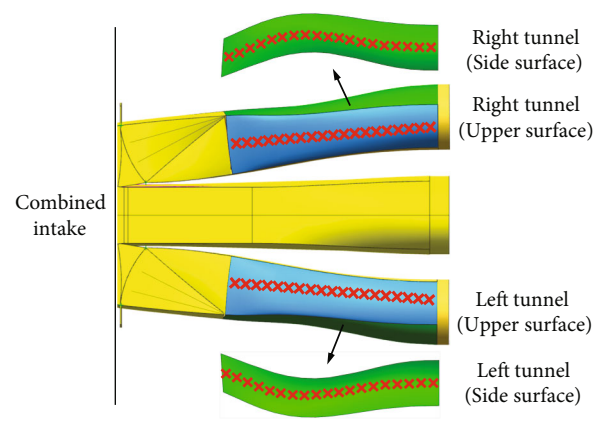

Figure 19: Layout of the pressure measurement points at the upper and side surface sections of the turbine dual tunnels (left and right).

From the results of the selected optimal measurement points in Figure 16, it can be observed that the selected points for each mode are relatively close to the throat. This indicates that these points can better reflect the backpressure at the exit of the isolator.

Based on the optimal measurement points of surface pressure extracted from each engine mode, we conduct 5-fold cross-validation for the prediction models. The dataset is also divided into the 80% training set and the 20% validation set. The results of the MAPE and R^2 are shown in Figure 17, where the average value and standard deviation of the error bar at per fold cross-validation are also given. It shows that the precision of the prediction models for each mode performs relatively well, with an average R^2 above 0.98 and MAPE within the range of 4% to 8%. Therefore, it can be indicated that the C_p-p_r prediction models have good generalization ability and maintain relatively high accuracy in cross-validation.

In practice, the inlet unstart usually occurs within milliseconds. For both the unstart warning and unstart state

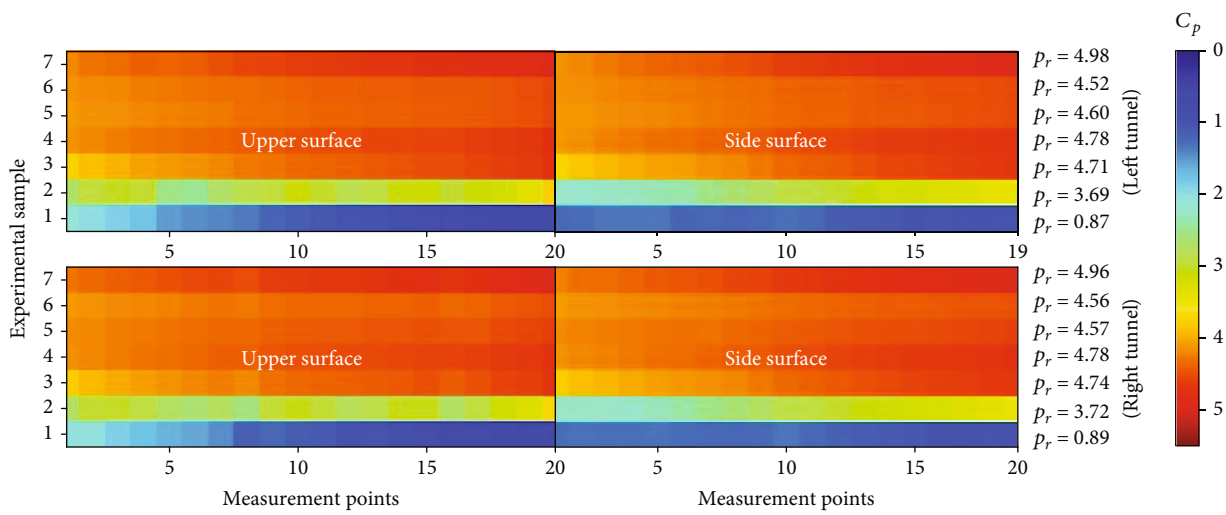

Figure 20: Thermograms of surface pressure coefficient from ground-based wind tunnel experimental data. It includes the upper and side surface sections of the turbine dual tunnels (left and right) and shows the corresponding backpressure ratios (numbered 1 to 7, with the inlet transition from start to unstart).

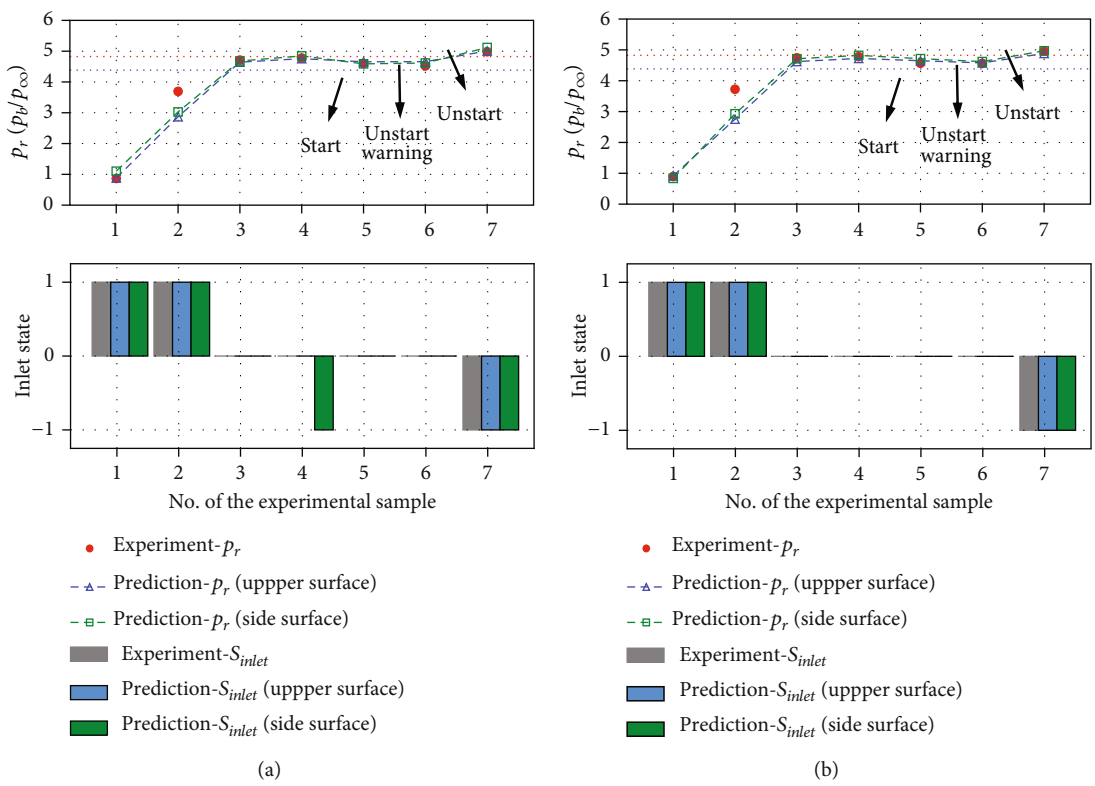

Figure 21: The comparison between the experimental and predicted results of the backpressure ratios and inlet states for the upper and side surface pressure dataset at Mach 2: (a) left turbine tunnel; (b) right turbine tunnel.

detection, the prediction efficiency of the models is also critical. The time cost for each C_p-p_r prediction model is shown in Figure 18. The training processes of models are conducted on the NVIDIA GeForce RTX 3050 graphics processing unit (GPU). It can be seen that the test time cost for each prediction model is within 1 to 2 ms, ensuring high prediction efficiency.

4.4. Experimental Validation of the Inlet Unstart Prediction and Warning. To validate the effectiveness of the inlet unstart prediction and warning method proposed in this study, Zhu et al. and Cai et al. [38, 39] conducted ground-based wind tunnel experiments in a follow-up study, where we obtain experimental data at Mach 2 in the TUR mode. The specific arrangement of measurement points of the

Table 5: Evaluation of backpressure ratio and inlet state prediction from the ground-based wind tunnel experimental data at Mach 2.

Turbine tunnel	p_r-R^2	p_r-MAPE	S_{inlet}-accuracy	Test time (ms)
Left tunnel (upper surface)	0.9438	0.0440	100.00%	9.6569
Left tunnel (side surface)	0.9577	0.0749	85.71%	9.2873
Right tunnel (upper surface)	0.9220	0.0512	100.00%	9.4883
Right tunnel (side surface)	0.9465	0.0491	100.00%	9.5605

turbine tunnels is illustrated in Figure 19, with 20 steady points on each upper surface and 19 steady points on each side surface. For each tunnel surface, seven experimental samples transitioning from the inlet start state to the unstart state are extracted, as depicted in Figure 20. The p_r for each experimental sample is shown in the figure, with two annotations indicating the backpressure ratios of the unstart states, which are 4.98 for the left tunnel and 4.96 for the right tunnel, both higher than the critical backpressure ratio ($p_u = 4.825$) predicted in Table 3.

Since the locations of the pressure measurement points may be different between the wind tunnel experiment and numerical simulation, we replaced the optimal combination of measurement points with those near [77, 82, 83] in Table 4. Figure 21 presents the comparison between the model predictions and experiment results for the backpressure ratios and the inlet states in both the left and right turbine tunnels. The statistical results of the predicted evaluation of the experimental samples under each surface of the turbine tunnels are given in Table 5. For the left tunnel, one sample incorrectly predicts the unstart warning state as an unstart state, whereas the predictions of the other samples are satisfactory. As for the right tunnel, the predicted inlet states on the upper and side surfaces matched the experiment results perfectly. The overall MAPE of p_r predicted by the C_p-p_r prediction models is no more than 7.5%, and the overall prediction accuracy for the inlet states reaches 96.43%.

From the above experimental results, it can be seen that the error of the C_p-p_r prediction model can be kept within a low range. The test time for the seven samples on each surface does not exceed 10 ms, with an average time cost of 1.3569 ms for single sample. The prediction of the inlet state is very close to the experiment results, with an overall deviation of 3.57%. Only one sample has prediction error due to a higher backpressure prediction. It is worth noting that in practice, the impact of a higher backpressure prediction is smaller than that of a lower one, which allows the model to predict the occurrence of unstart earlier. In summary, the unstart prediction and warning method in this paper exhibits excellent test performance in terms of prediction performance and time cost. It demonstrates the reliability and accuracy of the proposed method, despite the adjustment in the location of the measurement points between the wind tunnel experiment and numerical simulation.

5. Conclusions

In this paper, a backpressure unstart prediction and warning method is proposed for a combined cycle engine hypersonic inlet, and the implementation of the inlet unstart and unstart warning state detection for a wide speed range is discussed.

In the prediction of the critical backpressure ratios, this study accurately reveals at what backpressure ratio the inlet becomes unstart and warning based on numerical simulation. The overall average correlation coefficient of BP neural network regression on the test dataset at each working point is close to 0.99, indicating high accuracy. The inputs are determined by 10-CV SVM and the unstart margin, and the start/unstart state classification of inlet surface pressure at each working point had 100% accuracy, enabling accurate determination of surface pressure information at the unstart boundary and unstart warning boundary.

The conditions of critical backpressure ratios for the inlet unstart and unstart warning states are constructed by interpolation and three-dimensional fitting over the wide speed range. To a certain extent, the 10% unstart margin provides the safety range for the inlet unstart. In practice, the trained C_p-p_r prediction models by 1D-CNN, with the mean absolute percentage error of 4% to 8% on cross-validation evaluation, can be used for predicting the corresponding backpressure ratio only 2 to 4 measurement points required. It can be compared with the critical backpressure ratios on the fitting curves under the current freestream conditions to determine the inlet state. Finally, the proposed method is effectively validated by wind tunnel experimental data at Mach 2, and the model prediction error is no more than 7.5%. The average prediction time of a single sample is within 2 ms, and the prediction accuracy of the inlet state is as high as 96.43%. For further studies, the time-varying flow field as the more usual case will be considered, and the attempts will be made to conduct more operational conditions.

Abbreviations

H: High number
Ma: Mach number
C_p: Surface pressure coefficient
p: Static pressure
p_0: Total pressure
p_∞: Static pressure of the freestream
p_b: Backpressure at the exit of the isolator
p_s: Surface pressure of the inlet
p_r: Backpressure ratio
p_u: Backpressure ratio of the unstart state
p_{uw}: Backpressure ratio of the unstart warning state
S_{inlet}: Inlet state of prediction
y^+: The height of the first mesh cell off the wall in wall coordinate

α: Learning rate
γ: Decay rate for the learning rate
η: Unstart margin
TUR: Turbine
ERJ: Ejector ramjet
SCR: Scramjet
MT: Mode transition.

Data Availability

The data generated or analyzed during this study are available from the corresponding authors on reasonable request.

Conflicts of Interest

The authors declare that they have no conflicts of interest.

Acknowledgments

The authors would like to acknowledge the support of the National Natural Science Foundation of China (grant numbers U20A2069, 12302389, and 12372295).

References

[1] J. Urzay, "Supersonic combustion in air-breathing propulsion systems for hypersonic flight," *Annual Review of Fluid Mechanics*, vol. 50, no. 1, pp. 593–627, 2018.

[2] S. X. Liu, Z. H. Lin, B. B. Yan, W. Huang, and G. Choubey, "Wide-speed vehicle control considering flight-propulsion coupling constraints," *Journal of Aerospace Engineering*, vol. 36, no. 6, 2023.

[3] P. Dai, B. B. Yan, T. Han, and S. X. Liu, "Barrier Lyapunov function based model predictive control of a morphing waverider with input saturation and full-state constraints," *IEEE Transactions on Aerospace and Electronic Systems*, vol. 59, no. 3, pp. 3071–3081, 2023.

[4] S. X. Liu, B. B. Yan, W. Huang, X. Zhang, and J. Yan, "Current status and prospects of terminal guidance laws for intercepting hypersonic vehicles in near space: a review," *Journal of Zhejiang University: Science A*, vol. 24, no. 5, pp. 387–403, 2023.

[5] Z. Zhao, W. Huang, L. Yan, and Y. Yang, "An overview of research on wide-speed range waverider configuration," *Progress in Aerospace Sciences*, vol. 113, pp. 100606–100614, 2020.

[6] Y. F. Zhou, Z. X. Xia, D. Feng, and W. Huang, "Upgraded design methodology for airframe/engine integrated full-waverider vehicle considering thrust chamber design," *Acta Astronautica*, vol. 211, pp. 1–14, 2023.

[7] N. Viola, R. Fusaro, D. Ferretto, and V. Vercella, "Research, development and production costs prediction parametric model for future civil hypersonic aircraft," *Acta Astronautica*, vol. 204, pp. 58–72, 2023.

[8] Z. Y. Yin, Y. C. You, C. X. Zhu, J. F. Zhu, L. N. Wu, and Y. Huang, "The civil hypersonic multi-ducted twin-turbines ejector ramjet/scramjet combined cycle engine," *Acta Aeronautica et Astronautica Sinica*, vol. 44, no. 2, 2023.

[9] L. Shi, G. Zhao, Y. Yang et al., "Research progress on ejector mode of rocket-based combined-cycle engines," *Progress in Aerospace Sciences*, vol. 107, pp. 30–62, 2019.

[10] D. J. Dalle, J. F. Driscoll, and S. M. Torrez, "Ascent trajectories of hypersonic aircraft: operability limits due to engine unstart," *Journal of Aircraft*, vol. 52, no. 4, pp. 1345–1354, 2015.

[11] Y. Liu, L. Wang, and Z. S. Qian, "Numerical investigation on the assistant restarting method of variable geometry for high Mach number inlet," *Aerospace Science and Technology*, vol. 79, pp. 647–657, 2018.

[12] H. K. Liu, C. Yan, Y. T. Zhao, and S. Wang, "Active control method for restart performances of hypersonic inlets based on energy addition," *Aerospace Science and Technology*, vol. 85, pp. 481–494, 2019.

[13] W. Y. Su, Z. Hu, P. P. Tang, and Y. Chen, "Transient analysis for hypersonic inlet accelerative restarting process," *Journal of Spacecraft and Rockets*, vol. 54, no. 2, pp. 376–385, 2017.

[14] Q. F. Zhang, H. Chen, Z. Wu et al., "Experimental investigation of combustion-induced starting hysteresis in the scramjet," *Physics of Fluids*, vol. 34, no. 9, 2022.

[15] H. Kim, H. Seo, J. C. Kim, H. G. Sung, and I. S. Park, "A study on detection and quantification of a scramjet engine unstart," *Journal of the Korean Society for Aeronautical & Space Sciences*, vol. 50, no. 1, pp. 21–30, 2022.

[16] S. Walker, J. Sherk, D. Shell, R. Schena, and J. Gladbach, "The DARPA/AF Falcon program: the hypersonic technology vehicle # 2 (HTV-2) flight demonstration phase," in *15th AIAA International Space Planes and Hypersonic Systems and Technologies Conference*, pp. 2008–2539, Dayton, Ohio, USA, 2008.

[17] M. J. Bulman and A. Siebenhaar, "Combined cycle propulsion: aerojetinnovations for practical hypersonic vehicles," in *17th AIAA International Space Planes and Hypersonic Systems and Technologies Conference*, pp. 2011–2397, San Francisco, CA, USA, April 2011.

[18] C. Cox, C. Lewis, R. Pap et al., "Prediction of unstart phenomena in hypersonic aircraft," in *International Aerospace Planes and Hypersonics Technologies*, Chattanooga,TN,U.S.A, 1995.

[19] J. T. Chang, D. R. Yu, W. Bao, and L. Qu, "Influence factors of unstart boundary for hypersonic inlets," in *44th AIAA/ASME/SAE/ASEE Joint Propulsion Conference & Exhibit*, Hartford, CT, 2008.

[20] J. T. Chang, N. Li, K. Xu, W. Bao, and D. R. Yu, "Recent research progress on unstart mechanism, detection and control of hypersonic inlet," *Progress in Aerospace Sciences*, vol. 89, pp. 1–22, 2017.

[21] J. L. Wagner, K. B. Yuceil, A. Valdivia, N. T. Clemens, and D. S. Dolling, "Experimental investigation of unstart in an inlet/isolator model in Mach 5 flow," *AIAA Journal*, vol. 47, no. 6, pp. 1528–1542, 2009.

[22] J. L. Wagner, K. B. Yuceil, and N. T. Clemens, "Velocimetry measurements of unstart of an inlet-isolator model in Mach 5 flow," *AIAA Journal*, vol. 48, no. 9, pp. 1875–1888, 2010.

[23] W. Y. Su and K. Y. Zhang, "Back-pressure effects on the hypersonic inlet-isolator pseudoshock motions," *Journal of Propulsion and Power*, vol. 29, no. 6, pp. 1391–1399, 2013.

[24] H. J. Tan, L. Li, Y. Wen, and Q. F. Zhang, "Experimental investigation of the unstart process of a generic hypersonic inlet," *AIAA Journal*, vol. 49, no. 2, pp. 279–288, 2011.

[25] S. K. Im and H. Do, "Unstart phenomena induced by flow choking in scramjet inlet-isolators," *Progress in Aerospace Sciences*, vol. 97, pp. 1–21, 2018.

[26] S. Trapier, S. Deck, P. Duvcau, and P. Sagaut, "Time-frequency analysis and detection of supersonic inlet buzz," *AIAA Journal*, vol. 45, no. 9, pp. 2273–2284, 2007.

[27] J. T. Chang, L. Wang, B. Qin, W. Bao, and D. R. Yu, "Real-time unstart prediction and detection of hypersonic inlet based on recursive Fourier transform," *Proceedings of the Institution of Mechanical Engineers, Part G: Journal of Aerospace Engineering*, vol. 229, no. 4, pp. 772–778, 2015.

[28] S. Srikant, J. L. Wagner, A. Valdivia, M. R. Akella, and N. Clemens, "Unstart detection in a simplified-geometry hypersonic inlet-isolator flow," *Journal of Propulsion and Power*, vol. 26, no. 5, pp. 1059–1071, 2010.

[29] J. T. Chang, R. S. Zheng, L. Wang, W. Bao, and D. R. Yu, "Backpressure unstart detection for a scramjet inlet based on information fusion," *Acta Astronautica*, vol. 95, pp. 1–14, 2014.

[30] M. Mani and A. J. Dorgan, "A perspective on the state of aerospace computational fluid dynamics technology," *Annual Review of Fluid Mechanics*, vol. 55, no. 1, pp. 431–457, 2023.

[31] Y. F. Li, J. T. Chang, C. Kong, and W. Bao, "Recent progress of machine learning in flow modeling and active flow control," *Chinese Journal of Aeronautics*, vol. 35, no. 4, pp. 14–44, 2022.

[32] D. R. Yu, J. T. Chang, W. Bao, and Z. Xie, "Optimal classification criterions of hypersonic inlet start/unstart," *Journal of Propulsion and Power*, vol. 23, no. 2, pp. 310–316, 2007.

[33] J. T. Chang, D. R. Yu, W. Bao, and Y. Fan, "Operation pattern classification of hypersonic inlets," *Acta Astronautica*, vol. 65, no. 3-4, pp. 457–466, 2009.

[34] J. T. Chang, D. R. Y. Bao, Z. Xie, and Y. Fan, "A CFD assessment of classifications for hypersonic inlet start/unstart phenomena," *Aeronautical Journal*, vol. 113, no. 1142, pp. 263–271, 2008.

[35] J. T. Chang, Q. Hu, D. R. Yu, and W. Bao, "Classifier utility modeling and analysis of hypersonic inlet start/unstart considering training data costs," *Acta Astronautica*, vol. 69, no. 9-10, pp. 841–847, 2011.

[36] R. S. Zheng, J. T. Chang, H. He, and F. Chen, "Optimal classification of hypersonic inlet start/unstart based on manifold learning," *Applied Mechanics and Materials*, vol. 274, pp. 200–203, 2013.

[37] C. X. Zhu, X. Zhang, F. Kong, and Y. C. You, "Design of a three-dimensional hypersonic inward-turning inlet with triducts for combined cycle engines," *International Journal of Aerospace Engineering*, vol. 2018, Article ID 7459141, 10 pages, 2018.

[38] C. X. Zhu, H. Zhang, Z. C. Hu, and Y. C. You, "Analysis on the low speed performance of an inward-turning multiduct inlet for turbine-based combined cycle engines," *International Journal of Aerospace Engineering*, vol. 2019, Article ID 6728387, 10 pages, 2019.

[39] Z. J. Cai, Z. C. Hu, L. C. Yu, H. O. Tangbao, Z. H. Chengxiang, and Y. O. Yancheng, "Design concept and aerodynamic characteristics of XTER TBCC inlet," *Acta Aerodynamica Sinica*, vol. 40, no. 1, pp. 218–231, 2022.

[40] B. U. Reinartz, C. D. Herrmann, J. Ballmann, and W. W. Koschel, "Aerodynamic performance analysis of a hypersonic inlet isolator using computation and experiment," *Journal of Propulsion and Power*, vol. 19, no. 5, pp. 868–875, 2003.

[41] S. Salcedo-Sanz, J. L. Rojo-Álvarez, M. Martínez-Ramón, and G. Camps-Valls, "Support vector machines in engineering: an overview," *Wiley Interdisciplinary Reviews: Data Mining and Knowledge Discovery*, vol. 4, no. 3, pp. 234–267, 2014.

[42] M. Zeinali, S. Shahmorad, and K. Mirnia, "Hermite and piecewise cubic Hermite interpolation of fuzzy data," *Journal of Intelligent & Fuzzy Systems*, vol. 26, no. 6, pp. 2889–2898, 2014.